

## WAVEBAND LUMINOSITY CORRELATIONS IN FLUX-LIMITED MULTIWAVELENGTH DATA

J. SINGAL<sup>1</sup>, V. PETROSIAN<sup>2,3</sup>, J. HAIDER<sup>1</sup>, S. MALIK<sup>1</sup>

*Submitted to ApJ*

### ABSTRACT

We explore the general question of correlations among multiple different waveband luminosities in a flux-limited multiband observational data set. If such correlations are observed, they may either be intrinsic or induced by similar redshift evolution of the luminosities and/or the selection effects due to the flux limits. We first develop the question analytically, then use simulated observed flux-limited data sets with known luminosity correlations and evolutions to explore how the intrinsic nature of luminosity correlations can be deduced, including exploring the efficacy of partial correlation analysis with redshift binning in determining whether luminosity correlations are intrinsic. We use these techniques to show that the observed correlations between mid-infrared and optical luminosities in quasars are intrinsic to a greater degree than those observed between radio and optical luminosities. We then show that applying methods that we have developed in recent works can recover the true redshift luminosity evolutions, density evolutions, and local luminosity functions of populations observed in multiple flux-limited surveys in different wavebands, whether the luminosities in the wavebands are intrinsically correlated or not.

### 1. INTRODUCTION

When dealing with multiwavelength observations of astrophysical sources the question often arises whether the emissions in different wavebands (e.g. optical, radio, infrared, X-ray, gamma-ray, etc.) are correlated. Determining the intrinsic correlations between these emissions is crucial for addressing large variety of scientific questions, e.g. the relation between the emission processes and the sites and mechanisms of the acceleration of particles (or more generally the energizing of the plasma) responsible for these emissions. A common practice is to plot luminosities in two bands against each other for a sample of observed sources and determine the correlation empirically. However, more often than not such samples include sources with a large range of distances such as extragalactic sources with a range of redshifts.<sup>4</sup> Such samples are always subject to observational selection effects that truncate the data. The most common truncation arises in flux-limited data, where the fact that lower (higher) luminosities in both bands are dominated by sources at lower (higher) redshifts introduces a significant artificial correlation in the observed luminosities (e.g. Pavlidou et al. 2012; Antonucci 2011; Feigelson & Berg 1983; Khembavi et al. 1986; Chanan 1983). The situation is even more complicated, however, with extragalactic sources, where in addition to the observational selection effects, the different luminosities may undergo similar or different cosmological luminosity evolution which can itself cause correlations between different waveband luminosities (Petrosian & Singal 2015). Figure

1 shows two examples of *observed* luminosity correlations in two wavelengths in flux-limited data. The top panel is from an actual observed data while the bottom panel is from a simulated observed data set described below. In the latter case the population has no intrinsic luminosity-luminosity correlation by design yet displays a strong observed luminosity-luminosity correlation. Petrosian & Singal (2015), using partial correlation coefficients and Efron-Petrosian non-parametric methods (Efron & Petrosian 1992, 1999), showed that most but not all of the observed correlation in the top panel is induced by the selection process.

In this work we explore the question of to what extent observed correlations in multiwavelength flux-limited data are indicative (or not) of intrinsic correlations, and develop and verify techniques for directly determining correlations and distributions. In §2 we show analytically the extent to which i) truncations due to flux limits of the samples and/or ii) luminosity evolutions induce artificial correlation and the dependence of these effects on the characteristics of the luminosity functions (LFs).

It should be noted that the questions under considerations here are relevant not only for luminosity-luminosity correlations but are important for exploring the correlation, or generally the relation, between any two characteristics (or variables) both of which depend on and are obtained from the values of a third independent characteristic. In such a case partial correlation coefficients (based on, for example, Pearson or Kendall statistics) must be used as explored here. In astrophysical sources this applies to all extensive characteristics such as luminosity, mass or size, whose values can only be obtained with the measurement of their distances, which are subject to data truncation and in the case of extragalactic sources to cosmological evolutions mentioned above. Thus the procedures and results described here for luminosity-luminosity correlation is relevant for considerations of correlations between any two (similar or different) pairs of extensive characteristics.

jsingal@richmond.edu

<sup>1</sup> Physics Department, University of Richmond  
28 Westhampton Way, Richmond, VA 23173

<sup>2</sup> Kavli Institute for Particle Astrophysics and Cosmology  
SLAC National Accelerator Laboratory and Stanford University  
382 Via Pueblo Mall, Stanford, CA 94305-4060

<sup>3</sup> Also Departments of Physics and Applied Physics

<sup>4</sup> Exceptions arise in dealing with clusters of sources with sizes much smaller than their distance (e.g. Galactic star clusters, sources in distant individual galaxies or clusters of galaxies).

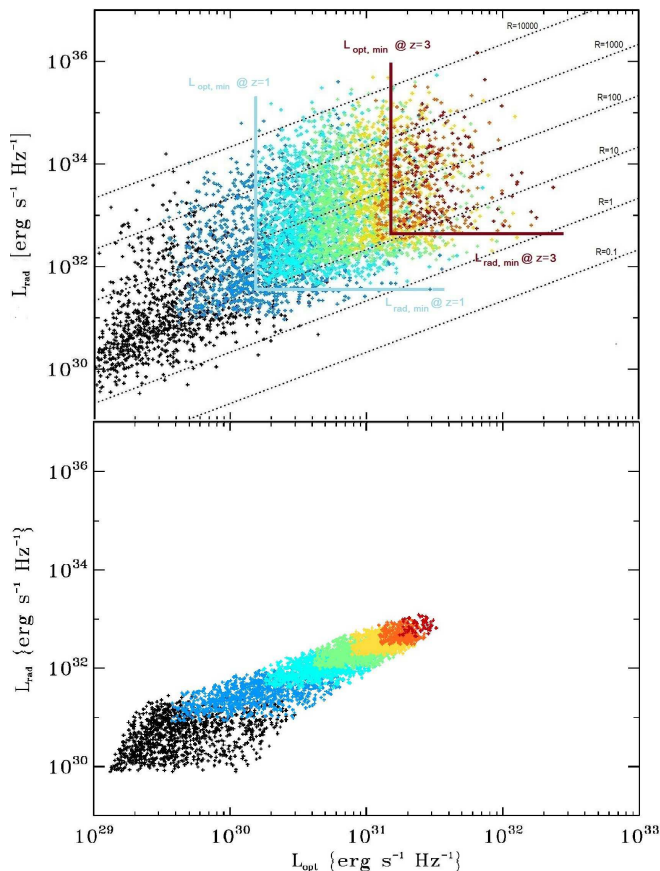


FIG. 1.— Two examples of observed luminosity-luminosity correlations in multiwavelength flux-limited data. Plotted are the 1.4 GHz rest frame radio luminosity density versus the 2500 Å rest frame optical luminosity density for quasars in a real (**top**) combined flux-limited radio-optical data set from Singal et al. (2013) and a simulated (**bottom**) combined flux-limited radio-optical data set subject to similar flux limits with known input parameters and *no intrinsic luminosity-luminosity correlation* developed in this work (discussed in §3). Colors represent different redshift bins. Black points are  $z \leq 0.5$ , dark blue points are  $0.5 < z \leq 1.0$ , light blue points are  $1.0 < z \leq 1.5$ , green points are  $1.5 < z \leq 2.0$ , yellow points are  $2.0 < z \leq 2.5$ , orange points are  $2.5 < z \leq 3.0$ , and red points are  $z > 3.0$ . Also shown for the real data are lines of constant raw  $R$  (defined as the ratio of the 5 GHz radio luminosity to the 2500 Å optical luminosity), and the limiting luminosities for inclusion in the sample at example redshifts of  $z = 1$  and  $z = 3$ . It is clear that selection and redshift evolutions can induce a correlation between the different waveband luminosities that is not intrinsic.

In §3 we introduce and explore simulated data sets with known intrinsic characteristics of the LF with different degrees of intrinsic correlation between different waveband luminosities. In §4 we explore the efficacy of partial correlation analysis with redshift binning in determining whether luminosity correlations are intrinsic, and show that the intrinsic correlations can be deduced by considering the correlations between the de-evolved luminosities. In §5 we demonstrate that techniques applied in recent works (Singal et al. 2011, 2012, 2014, 2013; Singal 2015; Singal et al. 2016), based on extensions of methods first proposed by Efron and Petrosian (Efron & Petrosian 1992, 1999) can recover the intrinsic distributions and correlations of the luminosities and redshifts in flux-limited multiwavelength data. We summarize the main results in §6.

## 2. ANALYTICAL CONSIDERATIONS

Let us consider the general trivariate luminosity function (LF)  $\bar{\Psi}(x, y, r)$  where  $x$  and  $y$  stand for dimensionless luminosities ( $\{x, y\} = L_{\{x, y\}}/L_0$ ), in two different photon energy bands, and  $r$  stands for a measure of the distance (in units of  $c/H_0$ ) of the object, such as redshift  $z$  or  $Z \equiv 1 + z$ , such as the co-moving distance

$$r = \int_1^Z dZ' / \sqrt{1 + \Omega_m(Z'^3 - 1)} \quad (1)$$

or luminosity distance  $r_L = rZ$ . In what follows we will use the last choice, i.e.  $r$  will stand for  $r_L$ .<sup>5</sup> The luminosities in a sample are calculated from the observed fluxes  $f_x, f_y$ . We express these dimensionless fluxes in units of fiducial flux  $f_0 = L_0/[4\pi(c/H_0)^2]$  so that we get  $\{x, y\} = r^2 f_{\{x, y\}}$ .

Without loss of generality we can write

$$\bar{\Psi}(x, y, r) = \Psi(x, y, r)\rho(r), \quad (2)$$

with  $\rho(r)$  describing the density evolution. The observed distribution of a sample of sources with flux limits  $f_{l,x}$  and  $f_{l,y}$  (in units of  $f_0$ ) is related to these intrinsic distributions as

$$d^3N/dx dy dr = (d\sigma/dr) \Psi(x, y, r) \Theta(x - x_m) \Theta(y - y_m) \quad (3)$$

where  $\Theta(x)$  is the step function ( $=1$ , for  $x > 0$  and  $=0$  otherwise), and the distance related distribution (cumulative density evolution) and limiting luminosities are given as

$$d\sigma/dr = \rho(r)(dV/dr), \quad x_m(r) = r^2 f_{l,x}, \quad y_m(r) = r^2 f_{l,y}. \quad (4)$$

For convenience we also define bivariate observed luminosity distribution

$$d^2N/dx dy \equiv N(x, y) = \int_0^\infty (d^3N/dx dy dr) dr \quad (5)$$

and mono-variate distributions

$$dN/\{dx, dy\} \equiv N(\{x, y\}) = \int_{\{x_m, y_m\}}^\infty N(x, y) d\{x, y\}, \quad (6)$$

and use the observed moments of these distributions to determine the correlation between the two luminosities. For example, we can determine if the observed average value of  $x$  depends on  $y$ :

$$\langle x(y) \rangle = \frac{\int_0^\infty x d^2N/(dx dy) dx}{dN/dy}. \quad (7)$$

We start first assuming that the luminosities are uncorrelated (i.e.  $x$  and  $y$  are independent) and see if data truncation induces a correlation in an observed sample. In this case we can separate the variables as  $\bar{\Psi}(x, y, r) = \psi(x)\psi(y)\rho(r)$ . Clearly in this case the intrinsic average values of variables are constants:

$$\langle x \rangle = \frac{\int_0^\infty x \psi(x) dx}{\int_0^\infty \psi(x) dx} = x_{\text{int}} = \text{Const.} \quad (8)$$

<sup>5</sup> Note that in a static Euclidean case (for example if one is dealing with Galactic or nearby extragalactic sources) all these measures of distance are equivalent.

In what follows we will consider several cases starting with the (mathematically) simplest case.

### 1. Simple Power law LFs and No Luminosity Evolution:

Here  $\psi(x) = \phi_x x^{-\delta_x} \Theta(x - x_0)$  (similarly  $\psi(y) = \phi_y y^{-\delta_y} \Theta(y - y_0)$ ). The no luminosity evolution implies that  $\phi_x, x_0$  and  $\delta_x$  are independent of  $r$ . The truncation due to flux limits introduces distances  $r_{0,x} = \sqrt{x_0/f_{l,x}}$  and  $r_{0,y} = \sqrt{y_0/f_{l,y}}$  below which the sample is not truncated. We assume that  $r_{0,x} < r_{0,y}$  and calculate the average value of  $x$  in the sample as a function of  $y$  (or vice versa in the opposite case). The intrinsic average value (for untruncated data)  $x_{\text{int}} = x_0(\delta_x - 1)/(\delta_x - 2)$  but for the truncated data average values is given as:

$$\langle x(y) \rangle = \frac{\int_0^{r_{0,x}} d\sigma \int_{x_0}^{\infty} dx x^{1-\delta_x} + \int_{r_{0,x}}^{\zeta r_{0,x}} d\sigma \int_{x_m}^{\infty} dx x^{1-\delta_x}}{\int_0^{r_{0,x}} d\sigma \int_{x_0}^{\infty} dx x^{-\delta_x} + \int_{r_{0,x}}^{\zeta r_{0,x}} d\sigma \int_{x_m}^{\infty} dx x^{-\delta_x}}. \quad (9)$$

where  $\zeta = (r_{0,y}/r_{0,x})\sqrt{y/y_0} > 1$ . In order to evaluate these integrals we need the functional form of  $d\sigma/dr$  which involves the product of two functions; the density evolution and the co-moving volume. In general this product is a complex function of any of the above three measures of distance ( $z, r, d_L$ ), in particular the last one being used here. Let us assume that we can approximate this with a power law,  $d\sigma/dr \propto r^{2+\alpha}$ , with  $\alpha$  presenting roughly an evolution index. We then have

$$\langle x(y) \rangle = x_{\text{int}} \times \frac{1 + (3 + \alpha) \int_1^{\zeta} \eta^{2+\gamma} d\eta}{1 + (3 + \alpha) \int_1^{\zeta} \eta^{\gamma} d\eta} \quad \text{with } \gamma = 4 + \alpha - 2\delta_x. \quad (10)$$

so that the result depends primarily on the index  $\gamma$ . For  $\gamma > -1$  ( $\alpha - 2\delta_x > -5$ ) the average value starts from near unity and rises quickly as  $\langle x(y) \rangle \propto y$  with increasing  $y$ , while in the opposite limit of  $\gamma < -3$  we get  $\langle x(y) \rangle \sim \text{const.}$ , and in between it varies more slowly than linearly with  $y$ . This indicates that in general data truncation induces some correlation between the luminosities and this correlation becomes stronger for larger values of the density evolution index  $\alpha$  and flatter LFs (smaller  $\delta_x$ ). This is as expected because both these effects result in a greater segregation of high and low luminosity sources at high and low redshifts, respectively, in the luminosity-luminosity scatter diagrams as shown in Figure 1.

### 2. Broken Power Law LFs

If broken power law applies only to one variable, say break of LF( $x$ ) at  $x_{\text{br}}$ , then as evident from the above analysis the shape of the other LF (namely  $y$ ) is unimportant, and the only complication is that in equation 9 we get three integrals in both the numerator and the denominator (the second integral gets divided into two at the break luminosity). As indicated above a steeper LF induces weaker correlation, thus we expect that a steepening of the LF at higher luminosities, which is often the case for most astronomical sources, will reduce this effect.

This can be seen by considering a very large steepening (i.e. a large increase in value of  $\delta_x$  instead of changes of order unity seen in AGNs) which essentially sets a ceiling for the average near a value at the break luminosity ( $\langle x(y) \rangle \rightarrow x_{r_{\text{mbr}}}$ ).

Now if the other LF also suffers a break (steepening at  $y_{\text{br}}$  as is common) then the integration limits become complicated depending on the relative values of the break luminosities and relative values of high luminosity indexes. In this case a numerical calculation, for specific parameters of the LFs, is required.

### 3. Effects of Luminosity Evolution

If the sources undergo luminosity evolution in one or both luminosities with forms  $x = x'g_x(r)$  and  $y = y'g_y(r)$ , where  $x'$  and  $y'$  will be referred to as the ‘‘local luminosities’’ if we normalize the evolution function so that  $g(0) = 1$ . As evident from above analysis the LF  $\psi(y)$  does not affect the average value of  $x$  but luminosity evolution in  $x$  alters the integrand in integration over the distance. If we carry out a variable change  $x' = x/g_x(r)$  we get an equation very similar to equation 9 with  $x$  replaced by  $x'$  and  $d\sigma/dr$  in the numerator changed to  $d\sigma/dr \times g_x(r)$ . This clearly adds the density evolution inducing an increase index of the  $\alpha$ , which as mentioned above increases the variation of the average  $x$  with  $y$  and the false correlation of the luminosities.

In summary, the above results show that for the types of LFs and luminosity evolutions seen in AGNs at various wavelength bands the truncation of the data due to observational selection effects induces an artificial correlation between luminosities the degree of which depends on the functional forms of the LFs and luminosity evolutions. The simulations below confirm these analytic results.

## 3. SIMULATED DATA SETS

In order to explore the effects of redshift evolutions and observational selection effects on populations with known intrinsic properties we simulate populations with luminosities in two different wavebands that are then observed with two hypothetical flux-limited surveys. To develop and highlight comparisons with recently explored real populations (e.g. Singal et al. 2013, 2016) we have assumed this simulated population to be ‘quasars’ observed by large area surveys and labeled the two wavebands ‘optical’ and ‘radio,’ but the conclusions as far as issues of luminosity-luminosity correlations and population distributions are entirely general.

### 3.1. Simulated Population Characteristics

We have distributed the populations according to the following intrinsic characteristics, now switching notation in some cases to be more concrete:  $L_a$  is the luminosity in a given waveband. The populations have intrinsic ‘‘local’’ (that is before any redshift evolution effects are considered) differential (and cumulative) luminosity functions which obey a simple power law of the form

$$\psi_a(L'_a) = -\frac{d\Phi(L'_a)}{dL'_a} = \psi_{0,a}(L'_a)^{\delta_a} \Theta(L'_a - L_{0,a}), \quad (11)$$

and introduce luminosity evolution with the functional form used for our AGN studies which has been shown to be a good fit to the data (Singal et al. 2013, 2016):

$$L_a(z) = L'_a \times g_a(z) \quad \text{with} \quad g_a(z) = \frac{Z^{k_a}}{1 + (Z/Z_{\text{CR}})^{k_a}} \quad (12)$$

where  $Z \equiv 1 + z$  as above, with potentially different parameters  $(\delta_a, L_{0,a}, k_a)$  for each waveband. The population also is simulated to have a co-moving density evolution  $\rho(z)$  or the differential number evolution

$$\frac{d\sigma(z)}{dz} = \rho(z) \frac{dV}{dz} \propto e^{-\frac{(z-z_m)^2}{2s}} \quad (13)$$

where  $\sigma(z)$  is the cumulative number evolution with  $z_m$  and  $s$  as the mean redshift and variance. With the population characteristics distributed in this way, the overall luminosity function in a waveband  $a$  can be expressed as

$$\bar{\Psi}_a(L_a, z) = \rho(z) \psi_a \left( \frac{L_a}{g_a(z)} \right) / g_a(z), \quad (14)$$

from which we can get the total number of observed objects to be

$$N_{\text{tot}} = \int_0^{z_{\text{max}}} dz \int_{L_{\text{min}}(z)}^{\infty} dL_a \rho(z) \frac{dV}{dz} \frac{\psi_a(L_a/g_a(z))}{g_a(z)}, \quad (15)$$

where the value of  $L_{\text{min}}(z)$  depends on the flux limit of the sample in waveband  $a$ .

In what follows we simulate a population in two different bands which we will call optical and radio with a simple power law intrinsic correlation between the local (prior to any redshift evolution) luminosities:

$$L'_{\text{rad}} \propto (L'_{\text{opt}})^\alpha \quad (16)$$

where  $\alpha$  is the correlation index. We explore the values  $\alpha = 0.0$  (i.e. no correlation) and two different degrees of correlations with  $\alpha = 0.5$  and  $1.0$ .

For the luminosity evolutions, in order to span values approximately matching the intrinsic characteristics of real populations from previous analyses, we adopt the value  $Z_{\text{CR}} = 3.7$  and  $k_{\text{opt}} = 3.0$  and  $k_{\text{rad}} = 4.5$ . For the luminosity functions and density evolution, also to approximate intrinsic values seen in previous analyses, we adopt power law indexes,  $\delta_{\text{opt}} = -2$  and  $\delta_{\text{rad}} = -2$ , and  $z_m = 2$  and  $s = 0.75$ . We also assume that the spectrum of sources in the short range of frequencies around each band can be approximated by a power law

$$L_a \propto \nu^{-\varepsilon_a} \quad (17)$$

with photon index values of  $\varepsilon_{\text{opt}} = 0.5$  and  $\varepsilon_{\text{rad}} = 0.4$ . We form Monte Carlo populations with these distributions by inverse transform sampling which allows random numbers to be generated uniformly on the interval  $[0,1]$  (e.g. Miller et al. 2010). For concreteness we consider the optical luminosity density at  $2500 \text{ \AA}$  and the radio luminosity density at  $1.4 \text{ GHz}$ .

### 3.2. Simulated Selection Effects

With the populations simulated according to the intrinsic characteristics of §3.1, we then apply simulated flux-limited “observations” in both wavebands. For simplicity, straightforwardness, and a connection to real

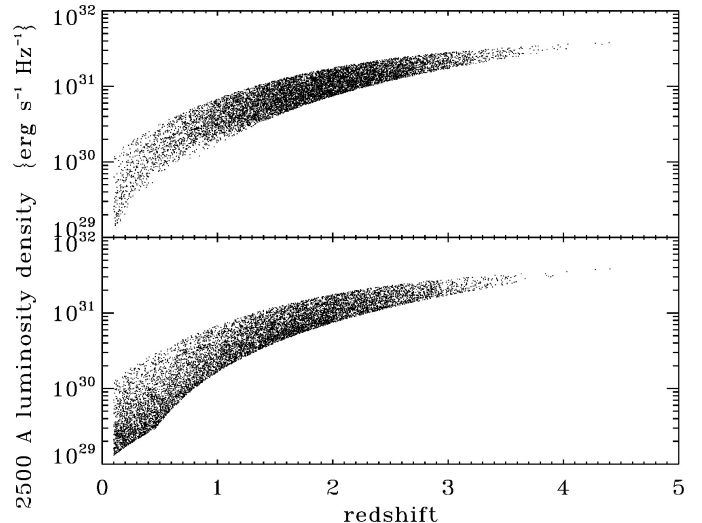


FIG. 2.— The optical luminosities vs. redshift for the observed simulated data sets, for the case of intrinsically correlated (**top** —  $\alpha = 1.0$ ) and intrinsically uncorrelated (**bottom** —  $\alpha = 0$ ) radio and optical luminosities.

data, the optical survey is taken to observe in a filter equivalent to the Sloan Digital Sky Survey (SDSS)  $i$  band (e.g. Schneider et al. 2010) and have a universal magnitude limit of 19.1 that band, and the radio survey is taken to be observing at  $1.4 \text{ GHz}$  and have a universal flux density limit of  $1 \text{ mJy}$ . The former is a simplified version of a limit that can be taken for the SDSS data release 7 quasar catalog (Schneider et al. 2010) and the latter is a simplified version of the limit of the Faint Images of the Radio Sky at Twenty one centimeters (FIRST) survey (Becker et al. 1995). The flux density for a given object  $j$  in waveband  $a$ ,  $f_{j,a}$ , is related to its luminosity density in that waveband by

$$f_{j,a} = \frac{L_{j,a} K_a(z)}{4\pi D_L(z)^2} \quad (18)$$

where  $D_L(z)$  is the luminosity distance determined from the standard cosmology and  $K_a(z)$  is the K-correction factor. For a power law spectrum as in equation 17 the K-correction factor is

$$K_a(z) = (1+z)^{1-\varepsilon_a} \quad (19)$$

Because an optical observation is needed to identify a quasar via colors and provide a spectroscopic redshift, only those objects whose flux density is greater than the corresponding limit in *both* wavebands is considered to be part of the observed sample. For ease of comparison we randomly select 10000 sources to comprise the observed sample in each case. In Figures 2, 3, 4, and 5 we show the optical luminosities vs. redshift, radio luminosities vs. redshift, radio luminosities vs. optical luminosities, and radio fluxes vs. optical fluxes, respectively, for the “observed” simulated data sets.

### 4. ANALYSIS WITH BINNED PARTIAL CORRELATIONS

Here we explore the efficacy of determining correlations with data binned in redshift. In the limit of infinitesimally narrow bins, the data within each bin should have no appreciable luminosity evolution and will be truncated parallel to the axes in the luminosity-luminosity plane, and therefore the phenomena that in-

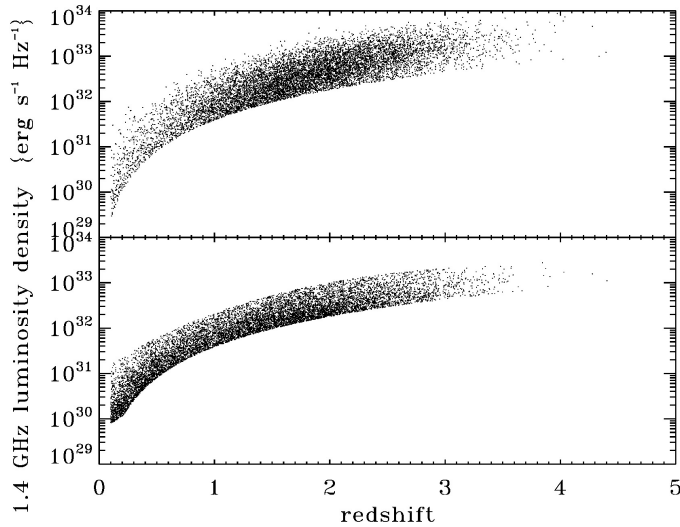


FIG. 3.— The radio luminosities vs. redshift for the observed simulated data sets, for the case of intrinsically correlated (**top** —  $\alpha = 1.0$ ) and intrinsically uncorrelated (**bottom** —  $\alpha = 0$ ) radio and optical luminosities.

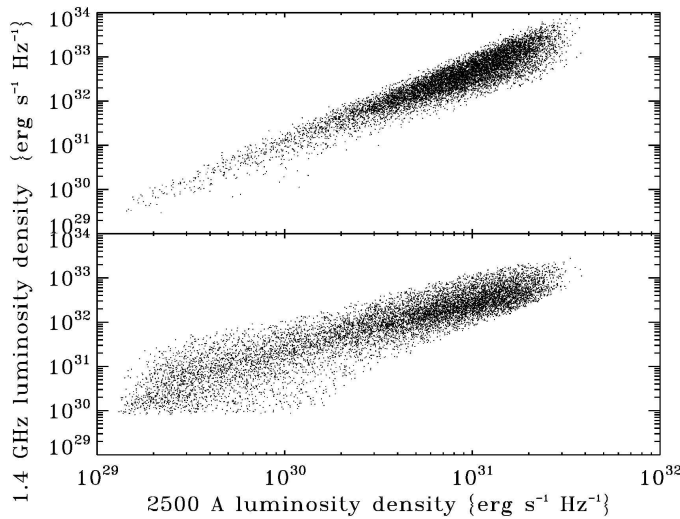


FIG. 4.— The optical vs. radio luminosities for the observed simulated data sets, for the case of intrinsically correlated (**top** —  $\alpha = 1.0$ ) and intrinsically uncorrelated (**bottom** —  $\alpha = 0$ ) radio and optical luminosities. As in Figure 1 it is clear that the *observed* luminosities can be correlated even if there is no intrinsic correlation between them.

duce luminosity-luminosity correlations discussed in §1 will be irrelevant. Thus redshift binning has been used as a technique to deduce intrinsic luminosity-luminosity correlations (e.g. Pavlidou et al. 2012). The question still arises, however, whether analysis in finite-sized bins where these effects do not disappear completely is effective.

A standard measure of partial correlations is the Pearson partial correlation coefficient (PPCC — e.g. Rao & Sievers 2007), which expresses the partial correlation between two variables discounting their mutual dependence on a third:

$$r_{12,3} = \frac{r_{12} - r_{13}r_{23}}{[(1 - r_{13}^2)(1 - r_{23}^2)]^{1/2}} \quad (20)$$

where  $r_{ab}$  is the standard sample product moment cor-

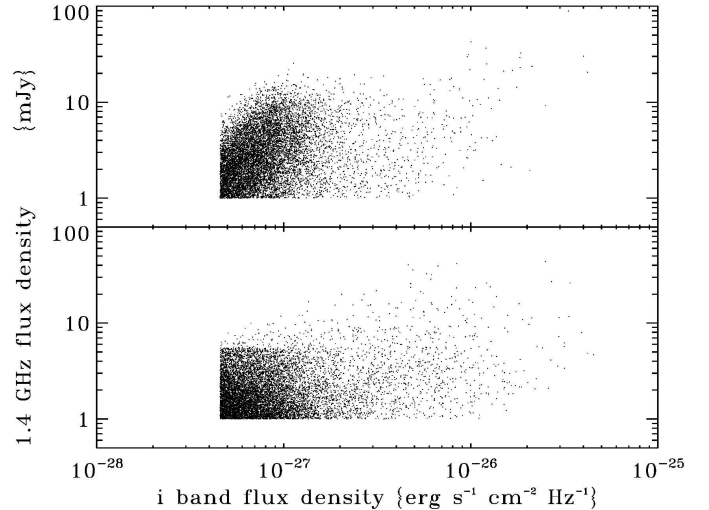


FIG. 5.— The *i* band optical vs. 1.4 GHz radio fluxes for the observed simulated data sets, for the case of intrinsically correlated (**top** —  $\alpha = 1.0$ ) and intrinsically uncorrelated (**bottom** —  $\alpha = 0$ ) radio and optical luminosities.

relation (PMC) between variables  $a$  and  $b$

$$r_{ab} = \frac{\sum_i (a_i - \bar{a})(b_i - \bar{b})}{N\sigma_a\sigma_b} \quad (21)$$

where  $\sigma_a = \sqrt{\frac{1}{N} \sum (a_i - \bar{a})^2}$  is the standard deviation of the  $a$  values and  $N$  is the total number of data points.

It is important to note that the PMC and PPCC are measures of the extent to which two variables are correlated, in the sense of being related by some function. However, they do not shed any light on the nature of the correlation function itself, and a higher value does not necessarily indicate a steeper correlation function, only that the data more closely adhere to the function whatever it may be. In this work we calculate PMCs and PPCCs based on the *logarithm* of the luminosities, in order to reduce the potential outside effect of a small number of objects with a very high luminosity in a given bin.

We bin the data and then examine a) the two luminosity-redshift correlations, b) the luminosity-luminosity correlation, and c) the *partial* luminosity-luminosity correlation for two cases: i) the raw observed luminosities, and ii) the so-called “local” luminosities with the best-fit redshift evolution removed. The differences between the luminosity-luminosity full and partial correlations between the two cases can reveal how much of the luminosity-luminosity correlation is physically real and how much is due to redshift evolution.

The most effective binning method for our needs, taking into consideration the data that we deal with, was found to be an equal number of objects per bin since objects are distributed unevenly across redshift. If we divide bins instead with uniform redshift size per bin, the few highest redshift bins end up with too few objects, resulting in unrealistic, erratic, and unreliable correlation coefficients for these bins. The number of objects in the least populated bins could be increased by increasing the width of the bins in redshift, but this leads to severely flux-limit induced correlations as discussed below. On the flip side, having an equal number of ob-

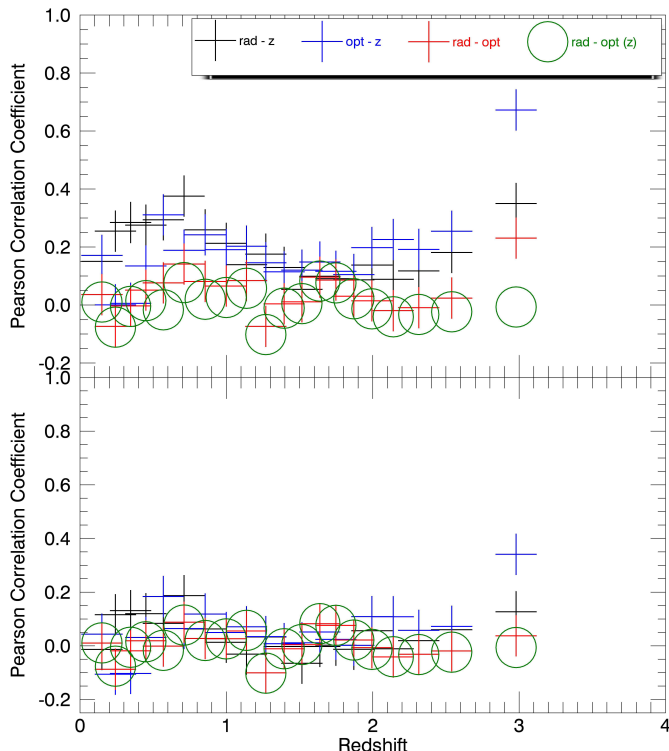


FIG. 6.— Radio-redshift, optical-redshift, and radio-optical PMCs, and radio-optical partial with redshift PPCCs in 20 bins of redshift with an equal number of objects per bin for raw (**top**) and local (**bottom**) luminosities for the intrinsically uncorrelated simulated observed radio and optical quasar data. Points are plotted at the average redshift and correlation values for each bin.

jects per bin and many bins would lead to bins with excessively small redshift ranges due to a high number of objects at those redshifts. While this does not make the luminosity-luminosity correlations unreliable, it does hide redshift-dependent correlations since the redshift range is too small to detect redshift dependent correlations. The optimum number of bins is thus the result of a trade-off between having some of the bins be too narrow and some too wide, and depends on the size of the data set.

#### 4.1. Partial Correlation Analysis with Simulated Data

Important considerations can be investigated by examining raw as well as local luminosities for the uncorrelated and correlated simulated data sets discussed in §3. For the best-fit redshift evolutions to achieve the local luminosities, we use evolutions of the form of equation 12 with the known input evolutions for the simulated data sets. Alternately, in the absence of this knowledge, the redshift evolutions could be determined with the methods of §5.1.

Figure 6 shows intrinsically uncorrelated simulated radio-optical data in 20 bins of redshift for both raw (top panel) and local luminosities (bottom panel). As expected, the radio-optical partial correlation coefficients for both raw and local luminosities are all approximately zero since this simulated data was designed to have no intrinsic correlation between the optical and radio luminosities. As hypothesized, in the top panel of Figure 6, we can see the radio-redshift and optical-redshift correlation coefficients to be non-zero since the populaion has

luminosity evolution. Since we are not using infinitesimally small redshift bins, there is an automatic influence of the flux-limit on the luminosities vis-a-vis redshift, which further contributes to a higher radio-redshift and optical-redshift correlation. Moreover, the radio-optical full correlation coefficients can be observed to be relatively higher than the partial correlation coefficients because the former are not disregarding their mutual dependence on redshift. This plot also demonstrates the contrast between using large versus small bins. The last bin in the top panel of Figure 6, at around average redshift of three, is the largest in redshift range since there are many fewer objects at higher redshifts. We can see that this bin has a relatively much higher observed dependence of the luminosities on redshift and thus has a higher radio-optical luminosity full correlation as well. This phenomenon was expected and is due to two reasons; one, as we discussed earlier, having larger redshift ranges brings in the flux-limit effect into the luminosity dependence on redshift, automatically and misleadingly strengthening the correlation between luminosities and redshift; and two, having a larger redshift range allows for a more accurate determination of the true correlation between the luminosities and redshift since with smaller redshift bins we potentially have an inadequate redshift range to extract an accurate correlation from.

In comparison, we expected luminosity dependence on redshift and thus the radio-optical full correlations to drop in the bottom panel of Figure 6 since the utilization of local luminosities removes the best-fit redshift evolution from the raw luminosities, allowing us to observe correlations that exist sans redshift dependence. This is exactly what is seen, as the full radio-optical and the partial radio-optical correlation coefficients align almost perfectly with each other in the bottom panel of Figure 6. However, local luminosities still do not remove the effect of the flux-limit, which is why we do not see a completely non-existent redshift dependence in luminosities, and which is why the last bin still has a relatively higher luminosity dependence on redshift than the other bins.

Figures 7 and 8 show the cases of intrinsically correlated simulated radio-optical data, with the correlation power law index (c.f. equation 16)  $\alpha=1.0$  and  $0.5$ , respectively, in 20 bins of redshift for both raw (top panel) and local luminosities (bottom panel), which manifests some distinctly contrasting features when compared to the uncorrelated cases. As anticipated, the radio-optical partial correlation coefficients for both the top and bottom panels of Figures 7 and 8 are all much higher than in Figure 6 since the simulated data was designed to have intrinsic correlation between the luminosities. The luminosity-redshift correlations are generally non-zero in the top panel of Figures 7 and 8 because of factors discussed earlier for the uncorrelated cases (i.e. an intrinsic luminosity-redshift dependence as well as flux-limit induced luminosity-redshift correlation), but drop lower (almost to zero) in the bottom panel of Figures 7 and 8 since using local luminosities removes their intrinsic dependence on redshift.

We see from considering these simulated data sets that full and partial correlation analysis in appropriately sized bins of redshift is a useful tool for determining presence or lack of, and at least qualitatively the degree, of intrinsic

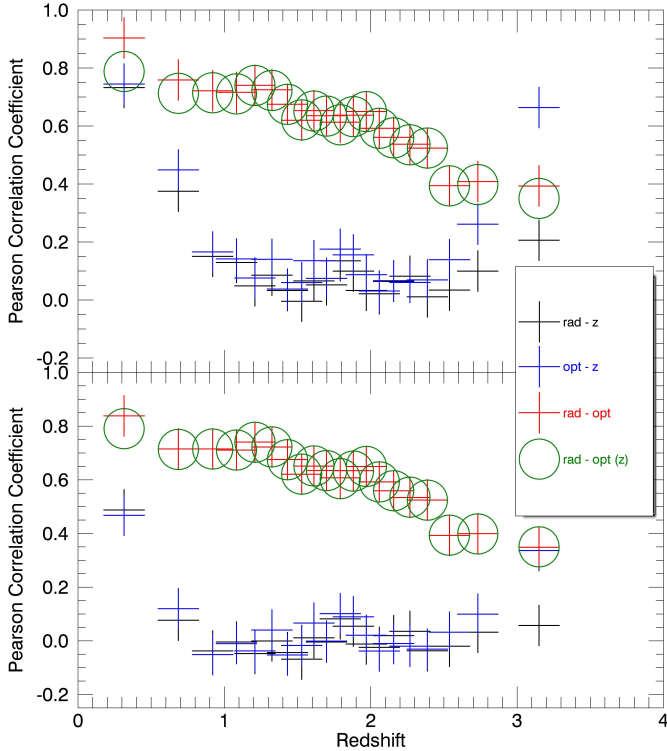


FIG. 7.— Radio-redshift, optical-redshift, and radio-optical PMCs, and radio-optical partial with redshift PPCCs in 20 bins of redshift with an equal number of objects per bin for raw (**top**) and local (**bottom**) luminosities for the intrinsically 1.0-correlated simulated observed radio and optical quasar data. Points are plotted at the average redshift and correlation values for each bin.

correlation between luminosities in a doubly flux-limited sample.

#### 4.2. Partial Correlation Results with Real Data

We now perform a partial correlation analysis with the real observed two-flux-limited data set of quasar optical and radio luminosities used in Singal et al. (2013), and the real observed two-flux-limited data set of quasar optical and mid-infrared luminosities used in Singal et al. (2016). The best-fit redshift evolutions for the luminosities of the form of equation 12 are determined in those works respectively, with methods verified here in §5.

Figure 9 shows the PMCs and PPCCs for the optical-radio data set with ten bins of redshift for both raw (top panel) and local luminosities (bottom panel). As this data set is quite a bit smaller than any of the simulated data sets or the optical-mid-infrared data set, a smaller number of bins is warranted as discussed above. As can be seen there, the radio-optical PPCCs are small yet not insignificant, with only two bins exhibiting radio-optical PPCCs equal to or less than zero. The radio-optical PMCs align almost perfectly with the PPCCs in the bottom panel of Figure 9, indicating that removing the redshift evolution removes almost all of the excess induced correlation between the luminosities. The radio-optical PPCCs maintain their magnitudes across both the panels of Figure 9, providing us a fairly reliable confirmation of the small yet not insignificant correlation between radio and optical luminosities.

Figure 10 shows real mid-infrared and optical data in 20 bins of redshift for both raw (top panel) and local

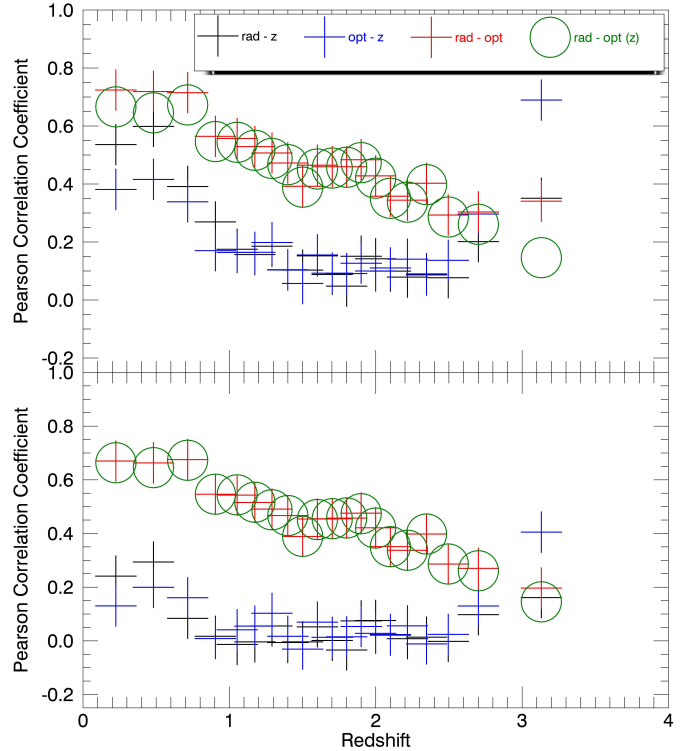


FIG. 8.— Radio-redshift, optical-redshift, and radio-optical PMCs, and radio-optical partial with redshift PPCCs in 20 bins of redshift with an equal number of objects per bin for raw (**top**) and local (**bottom**) luminosities for the intrinsically 0.5-correlated simulated observed radio and optical quasar data. Points are plotted at the average redshift and correlation values for each bin.

luminosities (bottom panel). Figure 10 can be observed to clearly have features quite similar to the case of intrinsically correlated simulated data, as shown in Figure 7. Figure 10 displays high luminosity-luminosity PMC and PPCC values across all bins, signifying a high intrinsic correlation between mid-infrared and optical radiation being emitted by the observed quasars. Once we remove the intrinsic redshift-evolution of the luminosities and use local luminosities (bottom panel of Figure 10), the infrared-optical PMCs drop slightly compared to the case of raw luminosities (top panel of Figure 10) and align almost perfectly with the PPCCs. This indicates that the non-intrinsic, flux-limit induced redshift dependence of the luminosities is almost negligible in all but the highest redshift bin, where even in the bottom panel the full infrared-optical PMC of the highest redshift bin is larger than the PPCC. This anomalous behavior predictably signifies that the highest redshift bin still has a non-intrinsic redshift dependence of luminosities owing to the relatively larger redshift range.

These results indicate that the mid-infrared and optical luminosities are highly intrinsically correlated whereas the radio and optical luminosities characterize a much smaller, although still present, intrinsic correlation. We briefly discuss the physical implications of this in §6.

#### 5. DEMONSTRATION OF NON-PARAMETRIC TECHNIQUES WITH SIMULATED DATA SETS

In recent works (Singal et al. 2011, 2012, 2014, 2013; Singal 2015; Singal et al. 2016) we used multiwavelength extensions of methods first proposed by Efron and Pet-

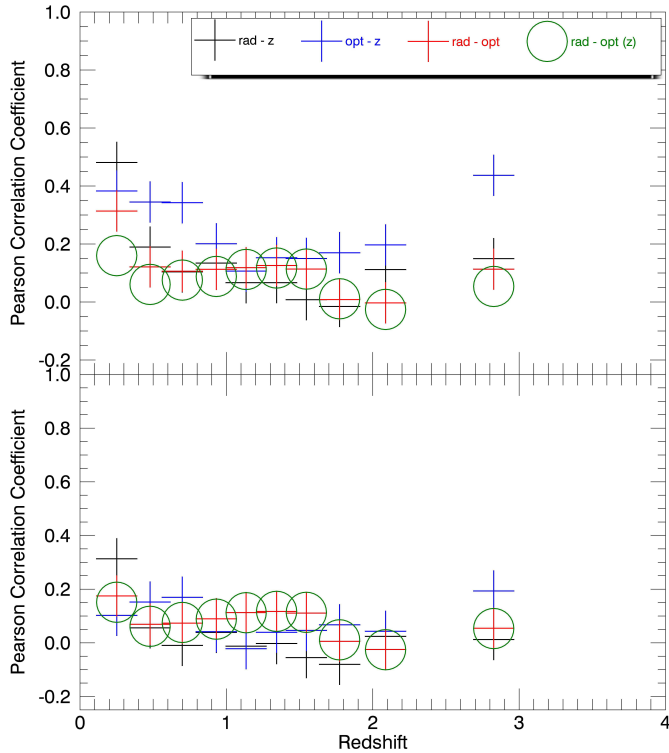


FIG. 9.— Radio-redshift, optical-redshift, and radio-optical partial with redshift PCCs in ten bins of redshift with an equal number of objects per bin for raw (**top**) and local (**bottom**) luminosities for the real observed radio and optical quasar data from Singal et al. (2013). Points are plotted at the average redshift and correlation values for each bin.

rosian (Efron & Petrosian 1992, 1999) to recover the intrinsic distributions and correlations of the luminosities and redshifts in flux-limited multiwavelength data. Here we apply these techniques to the simulated data sets developed in §3.

### 5.1. Redshift Evolutions

We determine the correlations between luminosity and redshift by using a variant of a rank test statistic modified with the use of *associated sets* which are unbiased sets for comparison. The test statistic

$$\tau = \frac{\sum_j (\mathcal{R}_j - \mathcal{E}_j)}{\sqrt{\sum_j \mathcal{V}_j}} \quad (22)$$

tests the independence of two variables in a dataset, say  $(x_j, y_j)$  for  $j = 1, \dots, n$ . Here  $\mathcal{R}_j$  is the dependent variable ( $y$ ) rank of the data point  $j$  in a set associated with it,  $\mathcal{E}_j = (1/2)(n + 1)$  is the expectation value and  $\mathcal{V}_j = (1/12)(n^2 + 1)$  is the variance, where  $n$  is the number of objects in object  $j$ 's associated set. For untruncated data (i.e. data truncated parallel to the axes) the set associated with point  $j$  includes all of the points with a lower (or higher, but not both) independent variable value ( $x_k < x_j$ ). If the data is truncated one must form the *associated set* consisting only of those points of lower (or higher, but not both) independent variable ( $x$ ) value that would have been observed if they were at the  $x$  value of point  $j$  given the truncation (see e.g. Singal et al. (2014) for a fuller discussion of these points).

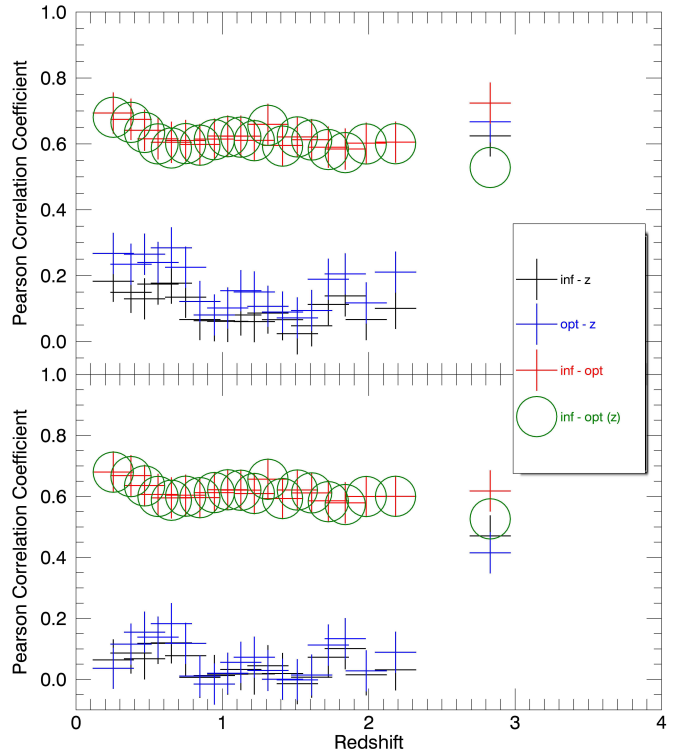


FIG. 10.— Mid-infrared-redshift, optical-redshift, and infrared-optical partial with redshift PCCs in 20 bins of redshift with an equal number of objects per bin for raw (**top**) and local (**bottom**) luminosities for real observed mid-infrared and optical quasar data from Singal et al. (2016). Points are plotted at the average redshift and correlation values for each bin.

If  $(x_j, y_j)$  are independent then the ranks  $\mathcal{R}_j$  should be distributed randomly and  $\tau$  should sum to near zero. Independence is rejected at the  $m\sigma$  level if  $|\tau| > m$ . To find the best fit correlation between  $y$  and  $x$  the  $y$  data are adjusted by defining  $y'_j = y_j/F(x_j)$  and the rank test is repeated, with different values of parameters of the function  $F$  until  $y'$  and  $x$  are determined to be uncorrelated.

In the case here of multiband luminosity and redshift data, for determining the redshift evolution of luminosity we can treat redshift as the independent variable and the luminosities as dependent variables. The problem becomes one of determining the evolution factors  $k_a(z)$  in the functions  $g_a(z)$  in equation 12 which render each luminosity uncorrelated with redshift. In the three dimensional case, properly taking into account the data truncations is important because we now are dealing with a three dimensional distribution  $(L_{\text{rad}}, L_{\text{opt}}, z)$  and two correlation functions ( $g_{\text{rad}}(z)$  and  $g_{\text{opt}}(z)$ ), plus we can find the true intrinsic correlation in this case because the truncation effects in the luminosity-redshift space are known and redshift is the independent variable in both cases.

Since we have two criteria for truncation, the associated set for each object  $k$  includes only those objects that are sufficiently luminous in both bands to have been in the survey if they were located at the redshift of the object in question. The luminosity cutoff limits for a given redshift must also be adjusted by factors of  $g_{\text{opt}}(z)$  and  $g_{\text{rad}}(z)$ . Consequently, we have a two dimensional mini-

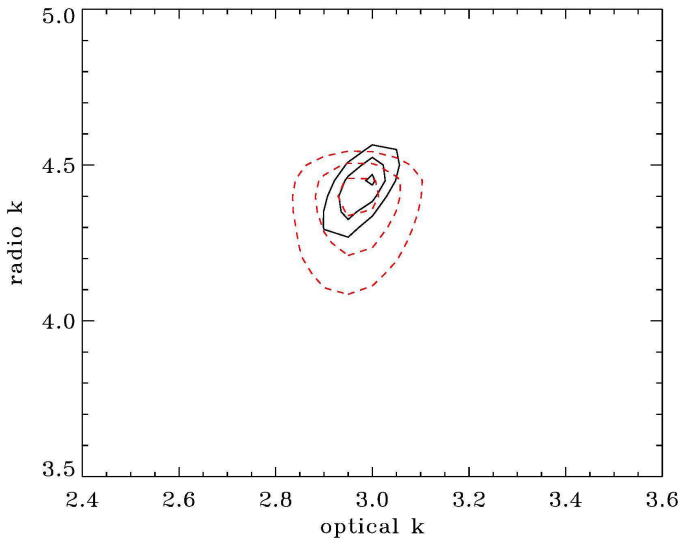


FIG. 11.— The  $1\sigma$ ,  $2\sigma$ , and  $3\sigma$  contours for the simultaneous best fit values of  $k_{\text{opt}}$  and  $k_{\text{rad}}$  of the simulated samples, for the forms of the luminosity evolutions given by equation 12, and for simulations with intrinsic (solid) and no intrinsic (dashed red) correlations between the luminosities. It is seen that the input intrinsic luminosity evolutions ( $k_{\text{opt}} = 3.0$  and  $k_{\text{rad}} = 4.5$  — see equation 12 in §3.1) are recovered to within small deviations.

mization problem, because objects will drop in and out of associated sets as  $g_{\text{opt}}(z)$  and  $g_{\text{rad}}(z)$  change, leading to changes in the calculated ranks in equation 22.

We form a test statistic  $\tau_{\text{comb}} = \sqrt{\tau_{\text{opt}}^2 + \tau_{\text{rad}}^2}$  where  $\tau_{\text{opt}}$  and  $\tau_{\text{rad}}$  are those evaluated considering the objects' optical and mid-infrared luminosities, respectively. The favored values of  $k_{\text{opt}}$  and  $k_{\text{rad}}$  are those that simultaneously give the lowest  $\tau_{\text{comb}}$  and, again, we take the  $1\sigma$  limits as those in which  $\tau_{\text{comb}} < 1$ . Figure 11 shows the 1 and 2  $\sigma$  contours for  $\tau_{\text{comb}}$  as a function of  $k_{\text{opt}}$  and  $k_{\text{rad}}$  for the simulated data sets. We see that the input intrinsic luminosity evolutions are recovered. We note here that we were able to recover the input intrinsic luminosity evolutions in the case of the intrinsically correlated luminosities without consideration of an orthogonal “correlation reduced” radio luminosity as explored in previous works (e.g Singal et al. 2013).

### 5.2. Density Evolution

One can define the cumulative density function

$$\sigma(z) = \int_0^z \frac{dV}{dz} \rho(z) dz \quad (23)$$

which, following Petrosian (1992) based on the method of Lynden-Bell (1971) which is equivalent to a maximum likelihood estimate, can be calculated by

$$\sigma(z) = \prod_j \left(1 + \frac{1}{m(j)}\right) \quad (24)$$

where the set of  $j$  includes all objects with a redshift lower than or equal to  $z$ , and  $m(j)$  is the number of objects with a redshift lower than the redshift of the object at redshift  $z$  which are in that object's associated set. In this case, the associated set is again those objects with sufficient optical and radio luminosity that they would be seen if they were at redshift  $z$ . The use of only the

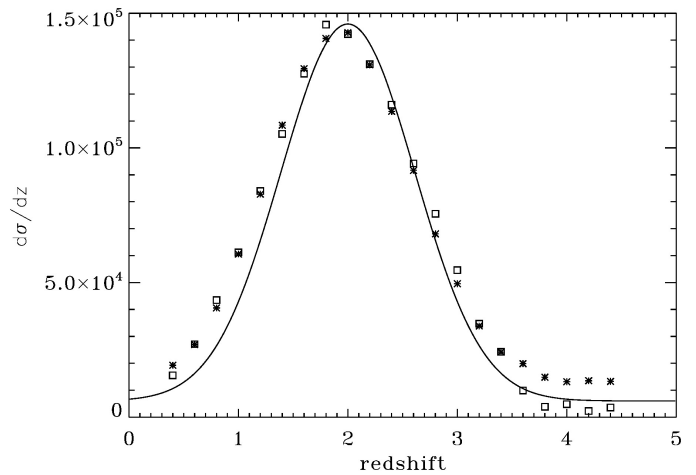


FIG. 12.— The differential density function  $d\sigma(z)/dz$  vs. redshift determined from the simulated data sets calculated as in §5.2, for the cases of intrinsic (stars) and no intrinsic (squares) correlations between the luminosities. The normalization of  $d\sigma(z)/dz$  here is arbitrary. It is seen that the input intrinsic redshift distribution of the population ( $z_m = 2.0$ ,  $s = 0.75$  — see equation 13 in §3.1) is relatively closely recovered. For reference a Gaussian function with these input distribution characteristics is also plotted. associated set for each object accounts for the biases introduced by the data truncation.

However, to determine the density evolution, the luminosity evolution determined in §5.1 must be taken out. Thus, the objects' optical and infrared luminosities, as well as the optical and infrared luminosity limits for inclusion in the associated set for given redshifts are scaled by taking out factors of  $g_{\text{opt}}(z)$  and  $g_{\text{rad}}(z)$  which are determined as above. The preceding method is fully adequate if there is a uniform selection function across redshift for quasars at a given flux. The differential density evolution  $d\sigma(z)/dz$  is shown in Figure 12. It is seen that the input intrinsic redshift distribution of the population is recovered.

### 5.3. Local luminosity functions

We first obtain a cumulative local luminosity function

$$\Phi_a(L'_a) = \int_{L'_a}^{\infty} \psi_a(L''_a) dL''_a \quad (25)$$

which, following Petrosian (1992) using the method of Lynden-Bell (1971),  $\Phi_a(L'_a)$ , can be calculated by

$$\Phi_a(L'_a) = \prod_k \left(1 + \frac{1}{n(k)}\right) \quad (26)$$

where  $k$  runs over all objects with a luminosity greater than or equal to  $L_a$ , and  $n(k)$  is the number of objects with a luminosity higher than the luminosity of object  $k$  which are in object  $k$ 's associated set, which in this case consists of those objects which would be in the survey if they were at object  $k$ 's luminosity considering the luminosity limits for inclusion in both optical and radio. The local luminosity function  $\psi_a(L'_a)$  is

$$\psi_a(L'_a) = -\frac{d\Phi_a(L'_a)}{dL'_a} \quad (27)$$

In §5.1 we determined the luminosity evolutions for the optical and radio luminosities. We can form the local optical  $\psi_{\text{opt}}(L'_{\text{opt}})$  and radio  $\psi_{\text{rad}}(L'_{\text{rad}})$  luminosity functions

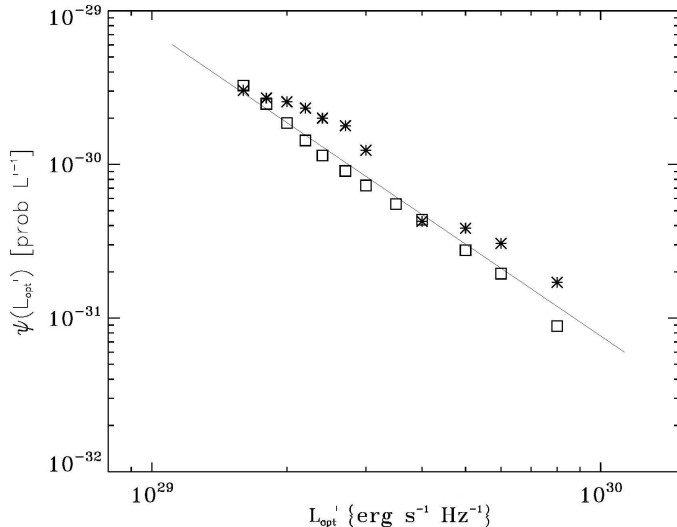


FIG. 13.— The local optical luminosity function  $\psi_{\text{opt}}(L'_{\text{opt}})$  for the simulated data sets, for the cases of intrinsic (stars) and no intrinsic (squares) correlations between the luminosities. It is seen that the input intrinsic local luminosity distributions of the populations ( $\delta_{\text{opt}} = 2.0$  — see equation 11 in §3.1) are recovered. For reference a line indicating a power law slope of  $\delta_{\text{opt}} = 2.0$  is shown.

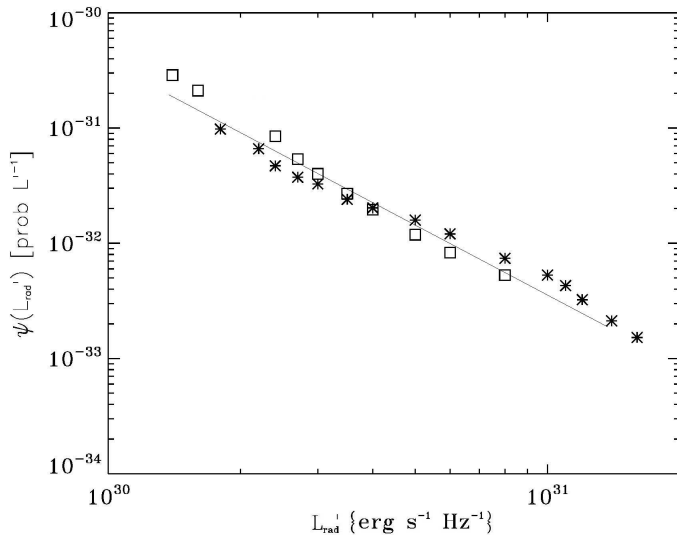


FIG. 14.— The local radio luminosity function  $\psi_{\text{rad}}(L'_{\text{rad}})$  for the simulated data sets, for the cases of intrinsic (stars) and no intrinsic (squares) correlations between the luminosities. It is seen that the input intrinsic local luminosity distributions of the populations ( $\delta_{\text{rad}} = 2.0$  — see equation 11 in §3.1) are recovered. For reference a line indicating a power law slope of  $\delta_{\text{rad}} = 2.0$  is shown.

straightforwardly, by taking the evolutions out. As before, the objects' luminosities, as well as the luminosity limits for inclusion in the associated set for given redshifts, are scaled by taking out factors of  $g_{\text{rad}}(z)$  and  $g_{\text{opt}}(z)$ , with  $k_{\text{rad}}$  and  $k_{\text{opt}}$  determined in §5.1.

Figures 13 and 14 show the local differential  $\psi_{\text{opt}}(L'_{\text{opt}})$  optical and radio luminosity functions respectively determined for the simulated data sets. Here we obtain the derivative of  $\Phi_a(L'_a)$  by fitting a simple cubic spline interpolation to  $\Phi_a(L'_a)$  and taking the derivative at various points where the spline is well behaved. We see that we recover the input intrinsic local luminosity functions.

## 6. DISCUSSION

Understanding the true correlation between luminosities in different wavebands is important for testing models in a variety of classes of extragalactic objects. However it is unavoidably the case that selection effects and the common positive redshift evolution of luminosity functions in different wavebands makes determining the actual presence or absence, and the extent, and the form, of the intrinsic correlation between different waveband luminosities for a class of objects from flux-limited survey data complicated. We showed in Figure 1 that even intrinsically uncorrelated data can manifest observed luminosity correlations, and developed this analytically for straightforward scenarios in §2. In the rest of this work, by considering simulated observational data with known input population correlations, luminosity functions, and evolutions as introduced in §3, we derived some results pertaining to the problem, and here and elsewhere have applied these techniques to real multiwaveband quasar and blazar data.

### 6.1. Partial Correlation Analysis

In §4 we determined via the simulated data sets that considering full and partial correlations in bins of redshift is a useful method for determining presence or lack of, and at least qualitatively the relative degree, of intrinsic correlation between two waveband luminosities in a doubly flux-limited sample. We then find there that for real data sets quasars manifest a very high degree of intrinsic correlation between mid-infrared and optical luminosities and a much lower degree of intrinsic correlation between radio and optical luminosities.

These results are interesting in the context of the models of how jets are launched by supermassive black holes and the multifaceted feedback effects in active galaxies between accretion disks, jets, and tori. In active galaxy systems, radio luminosity is thought to be dominated by jet emission while optical luminosity is either dominated by or at least significantly enhanced by accretion disk luminosity (e.g. Sikora et al. 2007; Broderick & Fender 2011). Mid-infrared emission, on the other hand, may be dominated by the brightness of a dusty torus which partially surrounds, and is heated by, the accretion disk (e.g. Lawrence 1991). In the so-called Blandford-Znajek mechanism, it is the spin energy of a supermassive black hole that is tapped for particle acceleration and therefore jet creation through a complex process that considers general relativistic and magnetohydrodynamic effects (Blandford & Znajek 1977; Blandford 1990). In light of this model, then, one would expect that larger black hole size, leading to a larger accretion disk, would correlate highly with brighter optical luminosity from the accretion disk and more mid-infrared luminosity from the heated torus, as well as brighter radio emission from the jets as more matter is available for the black hole to accelerate. On the other hand, one would hypothesize that faster black hole spin would affect primarily only the radio emission of these bands, as the radio emission alone of these is dominated by the strength of the jet in particular.

The very high degree of correlation seen in this analysis between mid-infrared and optical luminosities in quasars lends support to the picture of tori being heated by pri-

marily by accretion disks. The significantly weaker correlation between radio and optical luminosities can be taken to support the notion that radio emission is affected by both the accretion disk size and the black hole spin, and maybe most importantly by the latter. These results support an overall picture where black hole size determines accretion disk size and luminosity which then dominates the optical emission and becomes the primary driver of infrared emission via heating of the torus, while both black hole spin and size, and perhaps primarily spin, determine jet strength and therefore the radio luminosity.

### 6.2. Non-parametric Analysis

In §5 we determined with the simulated data sets that non-parametric statistical techniques first proposed by Efron & Petrosian (1992) and Efron & Petrosian (1999) and extended to multiwavelength analyses in recent works such as Singal et al. (2011), Singal et al. (2013), Singal et al. (2014), and Singal et al. (2016) can successfully recover the correct redshift evolutions of luminosities, redshift densities, and luminosity functions of extragalactic populations catalogued in flux-limited surveys. The above mentioned works have shown, among other conclusions, that active galaxy systems have manifest, among the wavebands considered, the most dramatic redshift evolution with luminosity in the gamma-ray band, followed by the radio band, followed by the optical band, with the least (although still positive) redshift

evolution of luminosity in the mid-infrared band. These results, with the highest redshift evolution of luminosity in the wavebands where emission is most closely tied to predominantly jet strength (radio and gamma ray), suggest that jet production mechanisms have become proportionally weaker over time compared to mechanisms that produce primarily optical and mid-infrared emission (such as accretion disk and torus brightness), again supporting the picture outlined above where black hole spin is heavily tied to jet production and the spin energy of black holes has been tapped for jet launching.

Funding for the SDSS and SDSS-II has been provided by the Alfred P. Sloan Foundation, the Participating Institutions, the National Science Foundation, the U.S. Department of Energy, the National Aeronautics and Space Administration, the Japanese Monbukagakusho, the Max Planck Society, and the Higher Education Funding Council for England. The SDSS Web Site is <http://www.sdss.org/>. This publication makes use of data products from the Wide-field Infrared Survey Explorer, which is a joint project of the University of California, Los Angeles, and the Jet Propulsion Laboratory/California Institute of Technology, and *NEOWISE*, which is a project of the Jet Propulsion Laboratory/California Institute of Technology. *WISE* and *NEOWISE* are funded by the National Aeronautics and Space Administration.

### REFERENCES

- Antonucci, R. 2011, ARA&A(arXiv:1101.0837)
- Becker, R., White, L., & Helfand, D. 1995, ApJ, 450, 559
- Blandford, R. & Znajek, R. 1977, MNRAS, 179, 433
- Blandford, R. 1990, "Physical Processes in Active Galactic Nuclei." in Active Galactic Nuclei, ed. T. J.-L. Courvoisier & M. Mayor (Berlin: Springer), 161
- Broderick, J. W., & Fender, R. P. 2011, MNRAS, 417, 184
- Chanan, G. 1983, ApJ, 275, 45
- Efron, B. & Petrosian, V. 1992, ApJ, 399, 345
- Efron, B. & Petrosian, V. 1999, JASA, 94, 447', Mill Valley, CA: University Science Books 1989
- Feigelson, E. & Berg, C. 1983, ApJ, 269, 400
- Khembavi, A., Feigelson, E., & Singh, K. 1986, MNRAS, 220, 51
- Lawrence, A., 1991, MNRAS, 252, 586
- Lynden-Bell, B. 1971, MNRAS, 155, 95
- Miller, F., Vandome, A., & McBrewster, J. 2010, "Inverse Transform Sampling." (VDM Publishing)
- Pavlidou, V. et al., 2012, ApJ, 751, 149
- Petrosian, V. 1992, in Statistical Challenges in Modern Astronomy, ed. E.D. Feigelson & G.H. Babu (New York:Springer), 173
- Petrosian, V., & Singal, J. 2015, "On the Relation Between AGN Jet and Accretion Disk Emissions." in Extragalactic Jets From Every Angle, Proc. IAU S313, eds. F. Massaro, C. C. Cheung, E. Lopez, A. Siemiginowska (Cambridge: Cambridge University Press)
- Rao, S., & Sievers, G. 2007, "A Robust Partial Correlation Measure." *Journal of Nonparametric Statistics*, 5, 1
- Richards, G. et al. 2006, AJ, 131, 2766
- Schneider, D., et al. 2010, ApJ, 139, 2360
- Sikora, M., Stawarz, L., & Lasota, J.-P. 2007, ApJ, 658, 815
- Singal, J., Stawarz, L., Lawrence, A., & Petrosian, V. 2011, "On the Radio and Optical Luminosity Evolution of Quasars." ApJ, 743, 104
- Singal, Petrosian, V., & Ajello, M. 2012, ApJ, 753, 45
- Singal, J., Stawarz, L., Lawrence, A., & Petrosian, V. 2013, ApJ, 764, 43
- Singal, J., Ko, A., & Petrosian, V. 2014, ApJ, 786, 109
- Singal, J. 2015, MNRAS, 115, 122
- Singal, J., George, J., & Gerber, A. 2016, ApJ, 831, 60
- White, R., Becker, R., Helfand, D., & Gregg., M. 1997, ApJ, 475, 479